Engineering Optimisation

Street Light Design Optimisation

Lorenz Veithen and Aleksandr Pavlov

TU Delft

DELFT UNIVERSITY OF TECHNOLOGY

FACULTY OF AEROSPACE ENGINEERING

ME46060

ENGINEERING OPTIMISATION: CONCEPTS AND APPLICATIONS

Engineering Optimisation Assignment

Street Light Design Optimisation

Lecturer: Dr. M. Langelaar
July 2, 2023

Task	Implementation	Documentation
Load model	A. Pavlov, corrected by L. Veithen	A. Pavlov
Stress/Deformation model	A. Pavlov, corrected by L. Veithen	A. Pavlov
Aerodynamic model	A. Pavlov	A. Pavlov
Light model	L. Veithen	L. Veithen, A. Pavlov
Constraints	L. Veithen	L. Veithen
Objective	L. Veithen	L. Veithen
Objective function characteristics	L. Veithen	L. Veithen
Monotonicity principle	A. Pavlov	A. Pavlov
Numerical noise	L. Veithen	L. Veithen
Objective sensitivity	L. Veithen	L. Veithen
(Local) optimisation setup	L. Veithen	L. Veithen
Local optimisers	L. Veithen	L. Veithen
L_1-L_2 optimisation	L. Veithen	L. Veithen
D_1-D_2 optimisation	L. Veithen	L. Veithen
Simplified optimisation analysis	L. Veithen	L. Veithen
Global optimisation setup	A. Pavlov	A. Pavlov
Global algorithm setup	A. Pavlov	A. Pavlov
Initial results	A. Pavlov	A. Pavlov
Optimum investigation	A. Pavlov	A. Pavlov
Sensitivity analysis	A. Pavlov	A. Pavlov
Conclusion and recommendation	A. Pavlov	A. Pavlov

Lorenz Veithen 5075211 | Aleksandr Pavlov 5003458

TU Delft Delft University of Technology

[1]Cover Image URL: https://unsplash.com/s/photos/street-light

1 Introduction

Lighting of highways plays a pivotal role in ensuring the safety of its drivers during night hours. These infrastructures enable drivers to see potential hazards beyond the reach of their car lights, permit them to see each other, and help them to navigate on the road safely [1]. With more than 2600km of highways to illuminate in The Netherlands, it is of the uttermost importance to reach an optimised structural and light spreading design to ensure a cost-effective implementation. This report aims to provide an overview of the optimisation process of the typical street light structural design to minimise costs, while maximising the illuminated area. To account for the former, the mass of the structure will be minimised.

Particularly, the optimisation process is focused on the structural integrity and the illumination conditions resulting from a single street light. The geometry of the problem is given in Figure 1.1, showing the seven design variables: L_1, D_1, t_1, L_2, D_2, t_2. All cross-sections are assumed to be hollow cylinders, the inclined pole is set at 95% of the vertical pole height, and the light source centre ray is perpendicular to the inclined pole direction. Furthermore, the thickness is assumed constant throughout the vertical and horizontal poles (but not especially equal between the two parts). This geometry is used as the starting point of all subsequent analysis. Additionally, the structure is assumed to be made of Aluminium 6061 T4, having the material characteristics given in Table 1.1.

Table 1.1: Aluminium 6061 T4 material characteristics [2].

Characteristic	**Value**
Density, ρ, [kg/m^3]	2700
Young's modulus, E, [GPa]	68.9
Shear modulus, G, [GPa]	26.2
Yield strength, σ_y, [GPa]	110
Shear yield strength, τ_y, [GPa]	55

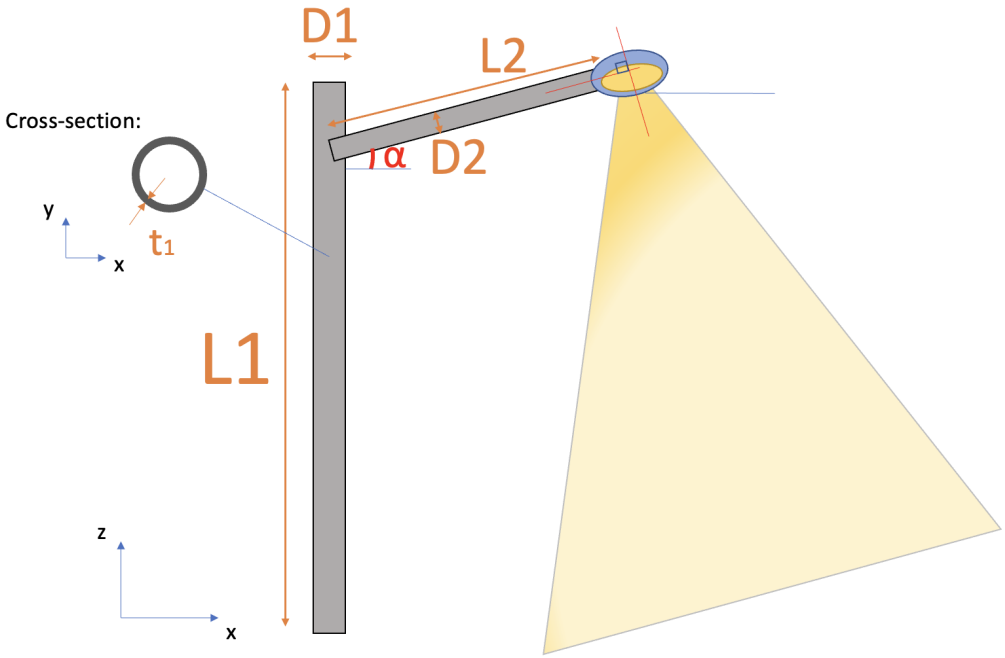

Figure 1.1: Schematic of the street light physical problem.

Problem Formulation 2

This chapter describes the model, constraints, and the objective tackled throughout this work.

2.1 Physical Problem Setup

The structure shown in Figure 1.1 is subject to loading due to the weight of the structure itself and the aerodynamic loading arising from the surrounding atmosphere. This loading will be analysed in the following subsections, for the vertical and inclined poles separately. Note that the most failure-critical points of the structure are at the roots of either poles (ground for the vertical section), as the loading compounds up to those points. Therefore, the model shown in the following does not consider the loading throughout the structure but only aims to determine the condition at those points (A and B in Figure 1.1).

To account for the worst-case scenario, the wind is modelled to be acting in the positive y-direction since in this case the horizontal pole is more exposed to the wind and hence the structure would experience a higher moment in the z-direction and more force carrying in the y-direction.

2.1.1 Inclined Section Loading

Firstly, the horizontal bar is taken to examine the total forces acting on it. In Figure 2.1, all the external forces are shown in purple being the horizontal bar's weight (W_h) and the wind force ($Fwind_h$), and the counter-balancing forces provided by the vertical support are shown in light blue colour. The magnitudes of the counter-balancing forces and moments were derived from force and moment equilibrium on the structure. Note that the exact attachment of the pole on the vertical section was not modelled, as a simplification. Furthermore, the weight is modelled as a single-point force at the centre of mass because its distributed load is known to be constant throughout the whole section.

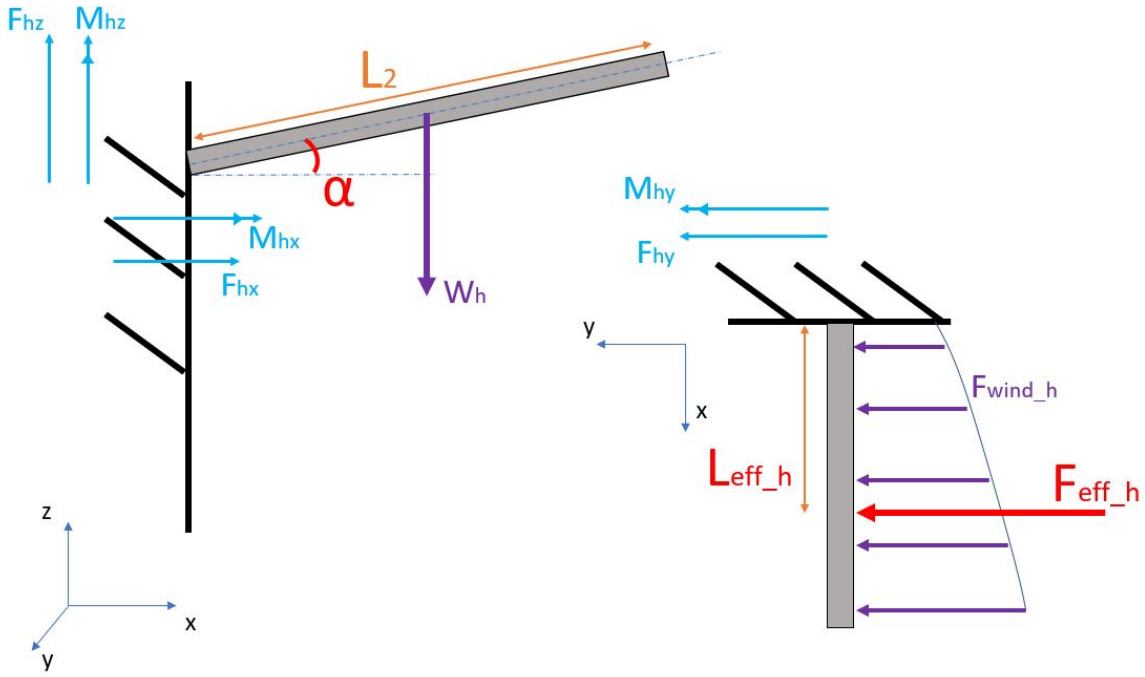

Figure 2.1: Loading on the inclined bar. Note that the top view is in the y-x plane, meaning that the figure is deformed for large values of α.

In the reference frame defined in Figure 2.1, the following reaction forces are derived. However, the forces acting on the cross-section of the inclined bar itself are slightly different: the weight force is decomposed in an axial ($R_h = W_h \sin\alpha$) and in-plane ($V_h = W_h \cos\alpha$) component.

$$F_{hx} = 0 \quad (2.1a) \qquad F_{hy} = -F_{\text{eff}_h} = -\int_0^{L_2} Fwind_h(x)dx \quad (2.1b) \qquad F_{hz} = W_h \quad (2.1c)$$

$$M_{hx} = 0 \quad (2.1d) \qquad M_{hy} = -W_h \frac{L_2}{2}\cos(\alpha) \quad (2.1e) \qquad M_{hz} = -F_{\text{eff}_h} L_{\text{eff}_h} \quad (2.1f)$$

$$L_{\text{eff}_h} = \frac{1}{F_{\text{eff}_h}} \int_0^{L_2} xFwind_h(x)dx \quad (2.2)$$

2.1.2 Vertical bar force counterbalance

Regarding the vertical bar, all the transferred moments from the inclined bar are now actively acting on the structure, and these forces are also needed to be counterbalanced by the base, shown in green in Figure 2.2. The vertical wind force (F_{effv}) and the effective length (L_{effv}) are found in the same way as for the inclined bar.

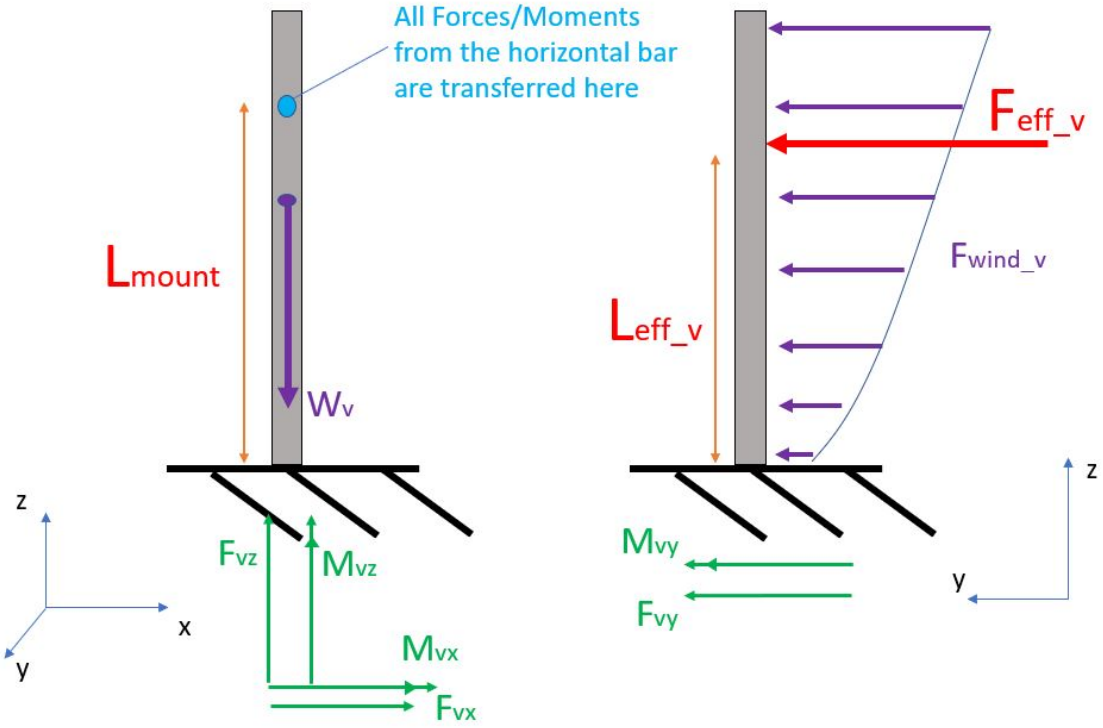

Figure 2.2: Loading on the vertical bar.

After identifying all the forces, the counter forces and moments have been computed as can be seen below, Equation 2.3. With this information, it is now possible to construct the model for the stresses experienced by the structure.

$$F_{vx} = 0 \quad (2.3a) \qquad F_{vy} = -F_{\text{eff}_h} - F_{\text{eff}_v} \quad (2.3b) \qquad F_{vz} = W_h + W_v \quad (2.3c)$$

$$M_{vx} = -F_{\text{eff}_h} L_{\text{mount}} - F_{\text{eff}_v} L_{\text{eff}_v} \quad (2.3d) \qquad M_{vy} = M_{hy} = -W_h(L_2/2)\cos(\alpha) \quad (2.3e) \qquad M_{vz} = M_{hz} = -F_{\text{eff}_h} L_{\text{eff}_h} \quad (2.3f)$$

2.2 Aerodynamic Modelling

The structure shall be able to sustain the most severe wind conditions in The Netherlands. According to the Dutch government, wind speeds up to 32.6 m/s refer to a very severe storm: number 11 on the Beaufort wind scale [3], and was assumed as a worst-case scenario to be sustained by the structure. For altitudes below 100m, it can be assumed that the structure is fully within the Planetary Boundary Layer (PBL) [4], meaning that viscous flow effects are dominant. As a simplification, the wind profile within the boundary layer is assumed to follow a power law, as described by Equation 2.4,

$$u = u_r \left(\frac{z}{z_r} \right)^{\beta} \tag{2.4}$$

where u is the wind speed (u_r is the reference speed), z is the altitudes and $\beta = 0.423$ is an atmosphere stability coefficient (value taken from [5] for a stable atmosphere). In this work, it is assumed that the wind velocity of 32.6m/s is reached at an altitude of 30m, hence fixing the law given by Equation 2.4. Having obtained the wind velocity as a function of the altitude, the aerodynamic force on the pole is computed by taking the drag force equation, which can be found in Equation 2.5,

$$F_{wind} = \frac{1}{2} \rho u^2 C_D A \tag{2.5}$$

where U is the wind velocity computed previously, and ρ is the air density assumed to be constant at a value of 1.225 kg/m^3, $C_D = 1.17$ is the drag coefficient of the structure [6] (3D subsonic cylinder), and the area $A = L \times D$[1] exposed to the airflow which is the projected area of the cylinder: a 2D rectangle.

In the numerical model produced, the wind force is numerically integrated on both the vertical (1) and inclined (2) poles. This results in a purely aerodynamic loading profile along both poles.

Regarding the inclined pole, the same procedure has been applied regarding the wind force calculation, and it has been discretised. To find which speeds apply for this section, the height of the mounting point (L_{mount}) has been taken as the starting altitude, and the final altitude is the Lh_{top} presented in Equation 2.6.

$$Lh_{top} = L_{mount} + L_2 sin(\alpha) \tag{2.6}$$

This function is running in a loop to create the wind speed profile up to the reference altitude, and then the relevant data points that are acting on the pole are taken, these points depend on the selected pole's vertical length.

2.3 Mechanical Modelling

To find stresses at the root points, the counterbalance forces and moments will be needed, but also the moment of inertia (I) and torsional moment of inertia (J). For the thin-walled circular section, those variables can be found by Equation 2.7 and Equation 2.8 where t is the thickness and d is the section's diameter [7]. The final structural property needed is the enclosed area A_m found by Equation 2.9, this will be needed for finding torsional stresses. Note that the I and J formulations are valid if $t_i/D_i < 0.1$ (model limitation which will be expressed as a constraint of the design).

$$I = \frac{\pi t d^3}{8} \tag{2.7}$$

$$J = \frac{\pi t d^3}{4} \tag{2.8}$$

$$A_m = \pi \left(\frac{d}{2} - \frac{t}{2} \right)^2 \tag{2.9}$$

2.3.1 Buckling

Euler buckling could become critical if the vertical pole becomes a long slender beam. For such a fixed-free system, $K = 2$, and the critical buckling force is given by,

$$F_{cr} = \pi^2 E I_1 / (K L_1)^2 = \pi^2 E I_1 / (2 L_1)^2 \tag{2.10}$$

2.3.2 Stresses

First, the stresses in the structure due to the loading described in Section 2.1.

2.3.2.1 Torsional Stress

Torsional stress is only acting on the vertical bar, with the highest magnitude being at the root. which can be found by Equation 2.11.

$$\tau_{\text{torsion,1}} = \frac{M_{vz}}{2 A_{m_1} t} \tag{2.11}$$

[1] L, the length of the element consider, and D the diameter of the pole

2.3.2.2 Shear Stress

This type of stress is found by Equation 2.11, where r is the radial distance from the cross-sectional centre. This type of stress is present in two directions for the horizontal bar, therefore the two stresses are combined as can be seen in Equation 2.13. For the vertical bar same equation applies, but only F_{vy} force acts as shear.

$$\tau_{\text{shear}_1} = \frac{2F_{1y}}{A_1} \tag{2.12}$$

$$\tau_{\text{shear}_2} = \sqrt{\left(\frac{2F_{\text{hy}}}{A_2}\right)^2 + \left(\frac{2F_{\text{hz}}\cos(\alpha)}{A_2}\right)^2} \tag{2.13}$$

2.3.2.3 Compressive Stresses

The only compression present is on the vertical bar, which can be found by Equation 2.15, where A is the cross-sectional area of the bar.

$$\sigma_{1z} = \frac{F_{vz}}{A_1} \tag{2.14}$$

$$\sigma_{2x} = \frac{W_h \sin(\alpha)}{A_2} \tag{2.15}$$

2.3.2.4 Stress due to bending

In both the horizontal and the vertical bar, two bending moments are acting on the structure which can be computed by Equation 2.16 and Equation 2.17.

$$\sigma_{bend_2} = \frac{M_{hy}r_2}{I_2} + \frac{M_{hz}r_2}{I_2} \tag{2.16}$$

$$\sigma_{bend_1} = \frac{M_{vx}r}{I_1} + \frac{M_{vy}r}{I_1} \tag{2.17}$$

2.3.2.5 Total Stress Environment

According to Hibbeler [7], the superposition principle should hold meaning that the stresses (σ) such as axial and bending are combined together. However, bending stress causes one side of the structure to experience tension and the other side compression. Considering that we have an axial load in compression due to weight, the most limiting stress experienced would be on the compressing side. To make sure that the two have the same sign absolute values were taken as seen in Equation 2.19.

$$\sigma_2 = |\sigma_{bend_2}| + |\sigma_{2x}| \tag{2.18}$$

$$\sigma_1 = |\sigma_{bend_1}| + |\sigma_{1z}| \tag{2.19}$$

Superposition also applies to the shear stresses (τ) such as torsion and shear are also combined together. Combining shear stresses in this way results in the worst-case scenario and there will be a side experiencing such shear force.

$$\tau_2 = |\tau_{\text{shear}_2}| \tag{2.20}$$

$$\tau_1 = |\tau_{\text{torsion}_1}| + |\tau_{\text{shear}_1}| \tag{2.21}$$

2.3.3 Deformations

It is undesirable that the streetlight is infinitely flexible since it would mean that the light source is not continuously shining at the desired place. Therefore a constraint on the maximum allowed deformation (y_{bend_max}) of $3cm$ is introduced and formulated in Subsection 2.5.2. To find how much each of the poles deflects, bending deflection equations were implemented from JPE [8].

In the case of the vertical pole, there is a deflection due to shear acting in the y-direction ($y_{\text{1bend\_sh}}$) which is the wind force acting on the pole. In every equation, the first term resembles the deflection at the point acting force or moment and the second term is an addition to resemble the deflection at the end of the pole. Similarly, there is also an imposed moment (M_{1y}) on the vertical pole from the inclined moment acting in the y-direction and causing it to deflect by ($y_{\text{1bend\_m}}$). Considering that both of the deflections are in the same direction, the sum of the terms is taken as a total deflection (y_{1bend}).

$$\begin{aligned}
y_{\text{1bend_sh}} &= \frac{F_{\text{eff_v}}L_{\text{eff_v}}^3}{3EI_1} + (L_1 - L_{\text{eff_v}})\sin\left(\frac{F_{\text{eff_v}}L_{\text{eff_v}}^2}{2EI_1}\right) \\
y_{\text{1bend_m}} &= \frac{M_{1y}L_{\text{mount}}^2}{2EI_1} + (L_1 - L_{\text{mount}})\sin\left(\frac{M_{1y}L_{\text{mount}}}{EI_1}\right) \\
y_{\text{1bend}} &= |y_{\text{1bend_sh}}| + |y_{\text{1bend_m}}|
\end{aligned} \tag{2.22}$$

Regarding the inclined pole, a similar principle applies. However, this time, the wind force and the inclined pole's weight are causing the deflection. These two deflections are in different directions therefore a magnitude of two terms is taken to find the total deflection of the inclined pole.

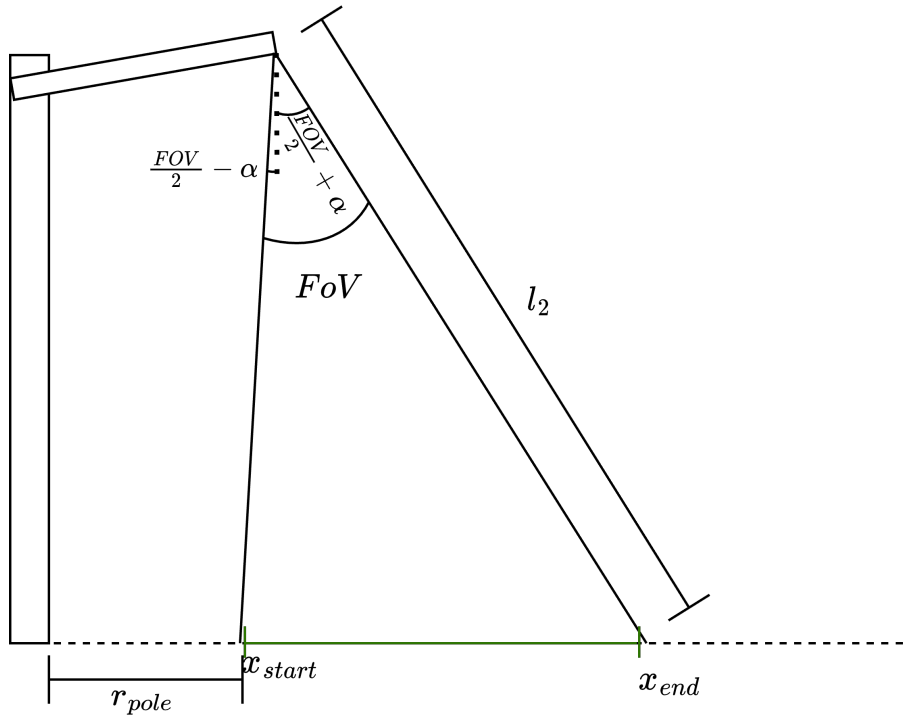

Figure 2.3: Geometry of the light conditions. The green part symbolises the road. Not to scale.

$$\begin{aligned} y_{\text{2bend\_sh}} &= \frac{F_{\text{eff\_h}} L_{\text{eff\_h}}^3}{3EI_2} + (L_2 - L_{\text{eff\_h}}) \sin\left(\frac{F_{\text{eff\_h}} L_{\text{eff\_h}}^2}{2EI_2}\right) \\ z_{\text{2bend\_weight}} &= \frac{F_{2z}\left(\frac{L_2}{2}\right)^3}{3EI_2} + \left(\frac{L_2}{2}\right) \sin\left(\frac{F_{2z}\left(\frac{L_2}{2}\right)^2}{2EI_2}\right) \\ z_{\text{2bend}} &= \sqrt{y_{\text{2bend\_sh}}^2 + z_{\text{2bend\_weight}}^2} \end{aligned} \tag{2.23}$$

Finally, there is also deflection due to torsion found by Equation 2.24, in radians. This deflection is also limited, as seen in Equation 2.35.

$$\theta_{\text{rot}} = \frac{M_{1z} L_{\text{mount}}}{GJ_1} \tag{2.24}$$

2.4 Light Modelling

The illumination of the road by the structure is modelled by a light cone with the endpoint of the inclined pole as an origin. The centre light ray is kept perpendicular to the inclined pole (as a design simplification), and a field of view (FoV) of 50deg is assumed[2]. The geometry of a typical lighting condition is shown in Figure 2.3, $r_{pole} = 1.25\text{m}$ was assumed. In the following section, constraints on the lighting conditions will be formulated to ensure that the road is completely illuminated (among others). The end and start positions of the light cone on the road are given by,

$$x_{start} = L_2 \cos(\alpha) - (L_{mount} + L_2 \sin(\alpha)) \tan\left(\frac{FoV}{2} - \alpha\right) \tag{2.25}$$

$$x_{end} = L_2 \cos(\alpha) + (L_{mount} + L_2 \sin(\alpha)) \tan\left(\frac{FoV}{2} + \alpha\right) \tag{2.26}$$

Furthermore, the scattering of the atmosphere is neglected in the model. The effect of scattering is expected to be small due to the relatively small distance covered by the light before reaching the ground. The energy reaching the ground is then determined based on Equation 2.27,

[2]This will be considered among the design constants to be investigated for the optimum sensitivity.

$$\Phi = \frac{Q_{lamp}}{4\pi l^2} \tag{2.27}$$

with Q_{lamp} being the power output the light source, and l the length of the light ray considered. The model set up only considers the first and last rays of the cone which reach the road, because one of them is the longest ray of the cone and therefore is the most constraining part of the light illumination. Following, the output power of the light source is typically around 30-50W[9], and will be assumed at a value of 30W for the nominal case considered in this work.

2.5 Constraints

A number of constraints apply to the design of such street light design. In the following section, those constraints are introduced and formulated mathematically. Note that 1's refer to the vertical pole, and 2's refer to the inclined pole. Additionally, it must be noted that those constraints were iterated upon using the global optimisation method from Chapter 5.

2.5.1 Environment and Manufacturing Constraints

Two main constraints arise from the road environment or the manufacturing capabilities. First, trucks shall be able to pass below the inclined part of the street light. This comes back to,

$$0 \geq 1 - \frac{L_{mount}}{L_{truck}} = g_1 \tag{2.28}$$

where the height of a typical truck, L_{truck} is taken equal to 4.3m. Following, the minimum manufacturable thickness of aluminium is at best $t_{min} = 0.5$ mm for performance grades[3]. This gives rise to,

$$0 \geq 1 - \frac{t_1}{t_{min}} = g_2 \tag{2.29a}$$

$$0 \geq 1 - \frac{t_2}{t_{min}} = g_3 \tag{2.29b}$$

Additionally, the inclined pole should be long enough to contain the light source. The minimum length is assumed to be $L_{2_{min}} = 0.1$m.

$$0 \geq 1 - \frac{L_2}{L2_{min}} = g_4 \tag{2.30}$$

Furthermore, the diameter of the inclined pole is assumed to be at most half of the diameter of the vertical pole, to ensure that a proper junction can be installed,

$$0 \geq \frac{(D_2/D_1)}{0.5} - 1 = g_5 \tag{2.31}$$

2.5.2 Mechanical Loading Constraints

A number of constraints arise due to the loading, stresses, and deformations acting on the structure. Note that for both the buckling and stress constraints, a safety factor, SF, of 1.5 is used. First, the vertical pole shall not buckle,

$$0 \geq \frac{Fvz}{(F_{cr}/SF)} - 1 = g_6 \tag{2.32}$$

Following, the material shall not yield (with a safety factor included) under the stress conditions. This is evaluated at the root of both the vertical and inclined pole, as those are the sections where the largest loading is present. The yield stresses in both axial and shear are written σ_y, τ_y,

$$0 \geq \frac{\sigma_2}{(\sigma_y/SF)} - 1 = g_7 \tag{2.33a}$$

$$0 \geq \frac{\tau_2}{(\tau_y/SF)} - 1 = g_8 \tag{2.33b}$$

$$0 \geq \frac{\sigma_1}{(\sigma_y/SF)} - 1 = g_9 \tag{2.33c}$$

$$0 \geq \frac{\tau_1}{(\tau_y/SF)} - 1 = g_{10} \tag{2.33d}$$

The last mechanical constraints to be taken into account arise from the deformation of the structure under the loading. For both poles the maximum allowed deflection is $3cm$, concerns $y_{\text{bend\_max}}$ and $z_{\text{2bend\_max}}$. The

[3]URL: https://www.materialise.com/en/academy/industrial/design-am/aluminum [online, accessed on 30/06/2023]

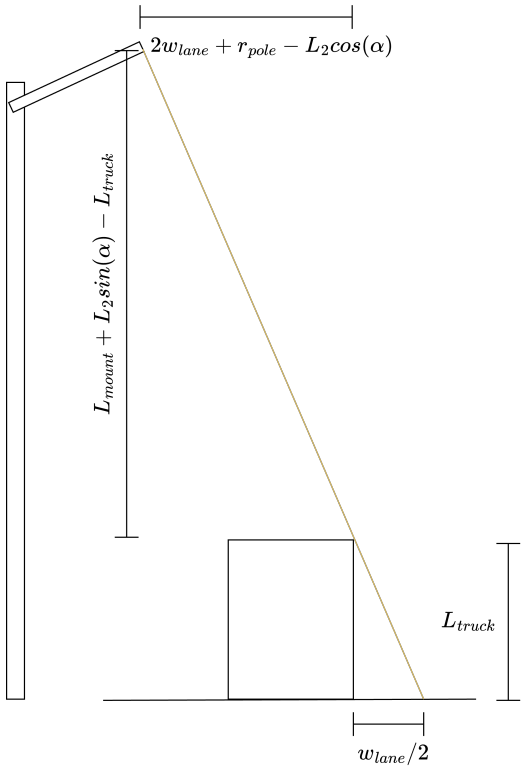

Figure 2.4: Geometry of the shadow due to a truck on the second lane.

deflections for each pole were found in Subsection 2.3.3 and subsequently resulted in the constraints presented in Equation 2.34.

$$0 = \frac{y_{\text{bend}}}{y_{\text{bend\_max}}} - 1 = g_{11} \quad \text{(2.34a)} \qquad 0 = \frac{z_{\text{2bend}}}{z_{\text{2bend\_max}}} - 1 = g_{12} \quad \text{(2.34b)}$$

Additionally, the angular deformation of the vertical pole is limited to 1°,

$$0 \geq \theta/\theta_{rot} - 1 = g_{13} \tag{2.35}$$

2.5.3 Lighting Constraints

A number of constraints apply to the design due to the lighting conditions to ensure a proper safety on the roads. Firstly, a number of geometrical considerations related to the coverage of the light beam are formulated. First, the start of the light cone should be before the start road and the end of the light pole should be after the road end (see Figure 2.3).

$$0 \geq \frac{x_{start}}{r_{pole}} - 1 = g_{14} \quad \text{(2.36)} \qquad 0 \geq 1 - \frac{x_{end}}{r_{pole} + w_{road}} = g_{15} \quad \text{(2.37)}$$

An additional constraint on the width of the light beam on the road was also formulated (although was found to be redundant later): $0 \geq 1 - (|x_{end} - x_{start}|)/w_{road} = g_{22}$, where x_{road} is the width of the road considered. Following, a truck could be passing on the road and causing some shadow on the lanes behind it. For safety reasons, this shadow shall not be covering more than half a lane, resulting in the constraint,

$$0 \geq \frac{\arctan\left(\frac{L_{truck}}{w_{lane}/2}\right)}{\arctan\left(\frac{L_{mount}+L_2\sin(\alpha)-L_{truck}}{2w_{lane}+r_{pole}-L_2\cos(\alpha)}\right)} = g_{16} \tag{2.38}$$

where the most constraining case was used (2nd lane with the height of truck). The constraint was determined based on Figure 2.4. Furthermore, it is required that the last light ray is not pointed too high with respect to the ground, which is expressed as,

$$0 \geq \frac{\alpha}{70\,\text{deg} - FoV/2} - 1 = g_{17} \tag{2.39}$$

At last, the average brightness required (B_{req}) for the motor vehicle lane of Class 1 is $2.93 \times 10^{-3} W/m^2$ [10], which was multiplied by a safety factor of 2. This gives rise to a constraint on both the first (18) and last rays (19) of the cone hitting the road

$$0 \geq \frac{\Phi}{B_{req}} - 1 = g_{18} \,\&\, g_{19} \tag{2.40}$$

2.5.4 Model Constraints

The model developed is only valid for thin-walled structures. Therefore, constraints imposing that the thickness is no larger than the diameter in each pole is formulated,

$$0 \geq \frac{t_1}{D_1} - 0.1 = g_{20} \tag{2.41a}$$

$$0 \geq \frac{t_2}{D_2} - 0.1 = g_{21} \tag{2.41b}$$

2.6 Optimisation Objective

Following the numerical model and the constraints detailed in the previous sections, the structure will be optimised to minimise its mass as a single-objective. The mass of the structure is given by,

$$M_1 = \left(\left(\frac{D_1}{2}\right)^2 - \left(\frac{D_1}{2} - t_1\right)^2\right)\pi L_1 \rho \tag{2.42a}$$

$$M_2 = \left(\left(\frac{D_2}{2}\right)^2 - \left(\frac{D_2}{2} - t_2\right)^2\right)\pi L_2 \rho \tag{2.42b}$$

$$M_{junction} = \left(\left(\frac{D_2}{2}\right)^2 - \left(\frac{D_2}{2} - t_2\right)^2\right)\pi \left(\frac{D_2}{2}\right)\tan(\alpha)\rho \tag{2.42c}$$

$$M_{ground} = 0.2 M_1 \tag{2.42d}$$

$$Objective : \min_{g_i} M = M_1 + M_2 + M_{junction} + M_{ground} \tag{2.43}$$

where Equation 2.42a gives the mass of the vertical pole, Equation 2.42b gives the mass of the inclined pole, Equation 2.42c gives the mass of the function (assuming that over the merging part, which has a length of $D_2 \tan(\alpha)$, the mass is equivalent to half of a cylinder), and Equation 2.42d gives the mass material in the ground to counterbalance the loading (assumed 20% of the vertical pole mass). The problem formulation will not be repeated for conciseness, but all constraints and objectives were given in the negative null form.

Considering the 7-dimensional optimisation problem, the objective is not expected to be convex everywhere due to the interplay between the variables (a sub-optimal solution could be given by a long inclined pole and a short vertical pole, which yields a smaller objective than both long inclined and vertical poles being long, but may still not be the global optimum).

Initial Problem Investigation 3

In this section, a brief investigation of the 7-dimensional problem is provided, with the aim to better understand the problem characteristics. This analysis shall permit to select more appropriate optimisation methods in the following sections.

3.1 Objective Function Characteristics

The objective function can be analysed as a function of the different design variables to determine specific characteristics, such as linearity, convexity, monotonicity, and boundedness. Figure 3.1 is obtained using the ranges shown in Table 3.1. It is clear that on the range of values considered, the objective show a monotonously increasing behaviour with respect to the dimensional variables of the structure. A larger inclined pole angle increases the weight of the structure slightly, but the effect is negligible compared to the other variables. Furthermore, while the behaviour of all variables seems linear due to the ranges considered, it can be seen from Equation 2.42 that the objective function is linear in L_1, L_2 and D_1; positively quadratic in D_2; negatively quadratic in t_1 and t_2 (although only infeasible thickness make the mass decrease); and tangent in α. This means that the mass of the structure is convex in all variables except t_1 and t_2.

Furthermore, Figure 3.1 shows that the objective needs to be bounded from below to ensure that it does not reach a zero value. This is taken care of by the constraints shown in the previous section, as shown in the next section.

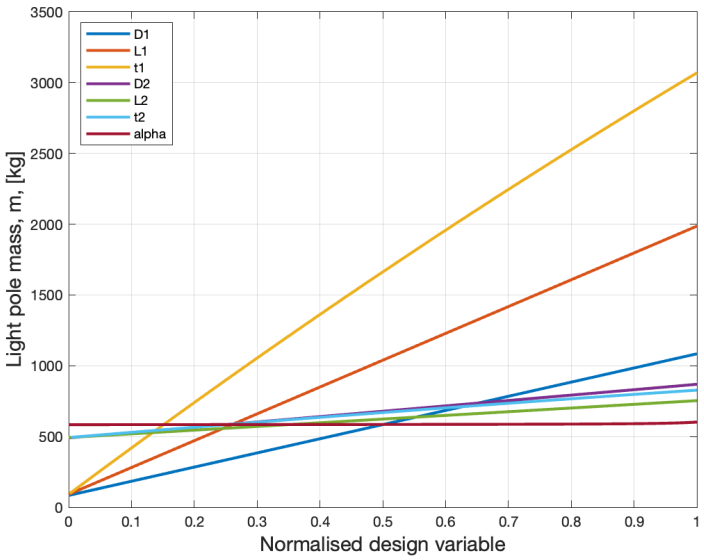

Figure 3.1: Objective function value as a function of normalised design variables.

Table 3.1: Ranges of values used to obtain Figure 3.1.

Variable	**Min**	**Max**
L_1 [m]	1E-4	50
D_1 [m]	1E-4	1
t_1 [m]	1E-4	0.05
L_2 [m]	1E-4	20
D_2 [m]	1E-4	1
t_2 [m]	1E-4	0.025
α	0°	85°

3.2 Applying the Monotonicity Principle

To check for monotonicity, as a first step the objective function is checked, for which variables it is increasing and for which it decreases. In the case of this problem, the objective function increases for each variable, which can be denoted by formulation in Equation 3.1. This means that in constraint evaluation, for each variable there must be at least one decreasing constraint (denoted by - superscript). Therefore such constraint evaluation was performed for each constraint and the results are summarised in the Table 3.2.

$$f(D_1^+, L_1^+, t_1^+, D_2^+, L_2^+, t_2^+, \alpha^+) \tag{3.1}$$

Table 3.2: Constraint Evaluation for Monotonicity

Table 3.3: Constraints 1-11

Constraint
$g_1(L_1^-)$
$g_2(t_1^-)$
$g_3(t_2^-)$
$g_4(L_2^-)$
$g_5(D_1^-, D_2^+)$
$g_6(D_1^-, L_1^+, t_1^-, D_2^+, L_2^+, t_2^+)$
$g_7(L_1^+, D_2^-, L_2^+, t_2^-, \alpha^+)$
$g_8(L_1^+, D_2^-, L_2^+, t_2^-, \alpha^-)$
$g_9(D_1^-, L_1^+, t_1^-, D_2^+, L_2^+, t_2^+, \alpha^+)$
$g_{10}(D_1^-, L_1^+, t_1^-, D_2^+, L_2^+, \alpha^+)$
$g_{11}(D_1^-, L_1^+, t_1^-, D_2^+, L_2^+, t_2^+, \alpha^-)$

Table 3.4: Constraints 12-22

Constraint
$g_{12}(L_1^+, D_2^-, t_2^-, \alpha^+)$
$g_{13}(D_1^+, L_1^-, t_1^+, D_2^-, L_2^-, \alpha^-)$
$g_{14}(L_1^-, L_2^+, \alpha^+)$
$g_{15}(L_1^-, L_2^-, \alpha^-)$
$g_{16}(L_1^-, L_2^-, \alpha^-)$
$g_{17}(\alpha^-)$
$g_{18}(L_1^+, \alpha^-)$
$g_{19}(L_1^+, L_2^+, \alpha^+)$
$g_{20}(D_1^-, t_1^+)$
$g_{21}(D_1^-, D_2^-, t_2^+)$
$g_{22}(L_1^-, \alpha^-)$

In the constraint evaluation, for each variable, there were multiple decreasing constraints. Meaning that there were no critical constraints and the problem is well-bounded. Some of the constraints, however, were redundant. For instance, constraint g_{22} specifies that the beam should cover the entire road. Whereas constraints g_{14} and g_{15} already specify that the beam's start and end, should hit the edges of the road. Such redundancies could be removed in future works on this problem to improve computational time.

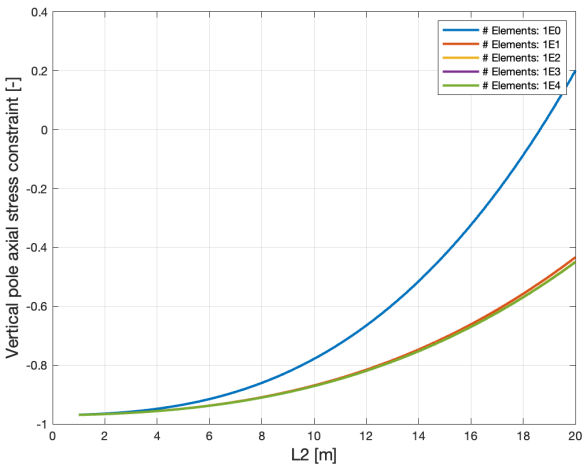

(a) Vertical pole axial stress constraint.

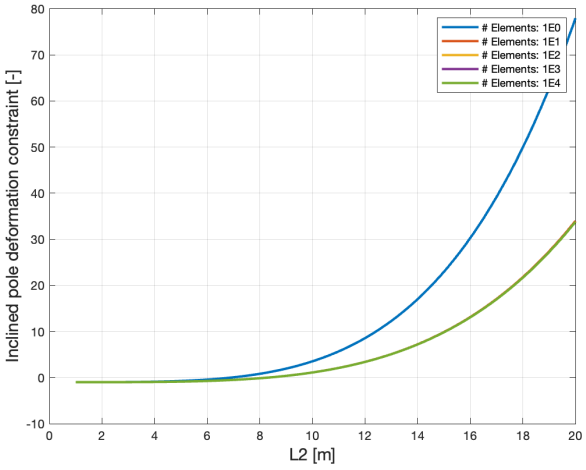

(b) Inclined pole deformation constraint.

Figure 3.2: Numerical noise assessment for two constraints related to the pole lengths.

3.3 Numerical Noise

The model described in the previous chapter only makes use of analytical equations and does not require any numerical methods using a discretisation of the domain (eg. Finite Element Methods, Finite Differences, etc.), with the exception of the numerical integration of the wind force on the structure. As this integration only affects the loading environment, and therefore the mechanical constraints of the model, only those are considered in the assessment of the numerical noise. Furthermore, those constraints are evaluated against their most relevant pole length, as the discretisation is performed along those variables only. The rest of the variables are kept constant with the values given in Table 3.5.

Table 3.5: Reference design in the design space.

Design variable	**Value**	**Design variable**	**Value**
L_1 [m]	13	L_2 [m]	7
D_1 [m]	0.5	D_2 [m]	0.25
t_1 [m]	0.0076	t_2 [m]	0.0063
α	10°	**Mass [kg]**	584.0692

No numerical noise was observed, as can be seen from Figure 3.2, where one example constraint for either pole is given as example. The response of the constraint functions remains smooth independently of the number of elements used in the numerical integration. Furthermore, the accuracy of the computation as a function of the number of elements used is considered through Figure 3.3, the error is obtained by comparing to the same simulation with 1E7 elements. Considering the simplifications made in the model, it becomes apparent that the use of 1000 elements is sufficient to obtain reliable results.

3.4 Objective Sensitivities

In this section, the relative importance of the design parameters on the objective function are determined using the problem logarithmic sensitivities around a reference design. The logarithmic sensitivity is given by,

$$\frac{d_L f}{d_L x} = \frac{d(log f)}{d(log x)} = \frac{x}{f}\frac{df}{dx} \tag{3.2}$$

which can be interpreted as a 'normalised' sensitivity of the objective function with respect to its inputs. The derivatives of the objective function $f = M$ with respect to each design variable are given in the appendix by Equation A.1, and the results of the logarithmic sensitivities are shown in Table 3.6.

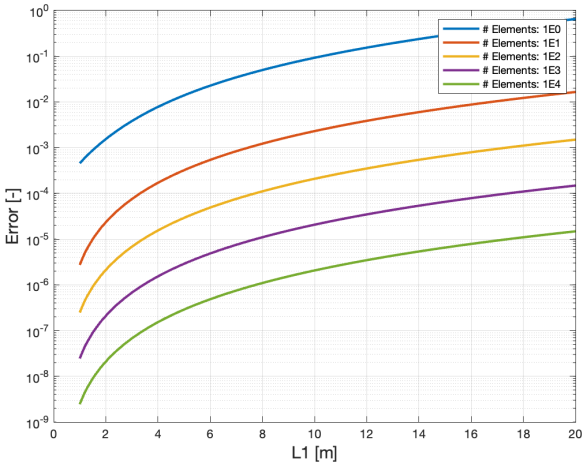

(a) Vertical pole axial stress constraint.

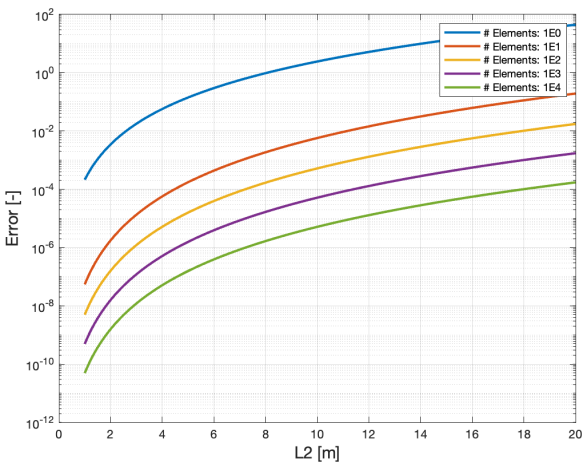

(b) Inclined pole deformation constraint.

Figure 3.3: Numerical accuracy assessment for two constraints related to the pole lengths.

Based on the results shown in Table 3.6, it is clear that the most influential components on the mass of the structure are the variables related to the vertical pole. Additionally, the angle of the structure has the least influence on the objective. However, the latter could open the design space to different types of designs, and is chosen to be kept as a variable. Furthermore, for each pole, their diameter are the most influential variables of the design, showing that it could be interesting to investigate those two variables in the optimisation of the simplified model.

Table 3.6: Logarithmic sensitivity around the reference design in Table 3.5.

Variable	$\frac{d_L f}{d_L x}$
D_1	0.8564
L_1	0.8434
t_1	0.8305
D_2	0.1611
L_2	0.1561
t_2	0.1525
α	0.0005

Simplified Optimisation 4

In this chapter, a simplified model is considered to better assess the characteristics of the problem, and determine preliminary solutions based on a few sets of two variables. Most notably, the lengths and diameters of the two beams will be considered. The former two because they dictate the overall shape of the structure, and the latter because they were found to be the most influential parameters for each beam. The rest of the design variables are kept constant, with the values of the reference design from Table 3.5, which lies in the design space.

4.1 Optimisation Setup

For the two sets of simplified optimisation considered (L_1 - L_2 and D_1 - D_2), the objective function is convex. The optimal will be found at the lowest value of each variable which can be taken based on the constraint, and no local minima can are found (as will be demonstrated below). Therefore, only local optimisation algorithms are considered in this section. This choice will be revisited in the next chapter, where the 7-dimensional function is not convex.

4.1.1 General Approach

The constraints were taken into account using a fitness function, using penalties to incentivise the algorithm of staying within the bounds of the design space. The optimisation problem is solved iteratively, by increasing the penalty by a factor of 10 at each iteration, from 1E3 to 1E10. Those iterations are necessary because the solution of a penalised optimisation problem lies outside the design space, and converges towards it if the penalty is increased. Furthermore, the penalty is not directly set to 1E10 to improve the convergence properties of the algorithm. The fitness function optimised for then becomes,

$$f = fitness = M + \sum_i p \ \max(0, g_i)^2 \tag{4.1}$$

where g_i's are the constraint functions of the problem, p is the penalty applied, and M is the objective (the mass of the structure). Through this transformation, the problem has then been converted into an unconstrained problem and can be treated as such. This approach was preferred above working with the KKT conditions due to its simple, yet effective, implementation.

4.1.2 Implemented Algorithms

A number of algorithms were implemented to solve the unconstrained problem: a gradient computation, a line search algorithm (golden search), and two unconstrained optimisation algorithms (Conjugate Gradient and BFGS).

4.1.2.1 Gradient Computations

The gradient of the objective function was implemented for the 7-dimensional problem, with the possibility to reduce the dimensionality for the analysis in this chapter. The gradient vector is computed using a Central Finite Difference scheme by varying each component with a relative change of 1E-5 independently,

$$\nabla \vec{f_i} = \frac{f(x_i + \delta) - f(x_i - \delta)}{2\delta} \tag{4.2}$$

$$\delta = (\text{1E-5})x_i + \text{1E-8} \tag{4.3}$$

The finite difference scheme was preferred above the analytical or semi-analytical approaches due to the use of the fitness function with penalties, making it more difficult and time-consuming to determine the derivatives. The finite difference method provides an easy-to-implement and versatile definition of the gradient, despite being less efficient. Due to the simplicity of the model, the lack of efficiency was not found to be a problem throughout this work.

4.1.2.2 Golden Search

To ensure a correct and fast convergence of the BFGS and Conjugate Gradient (CG) algorithms, a line search method was implemented. Three options were considered: dichotomous search, Fibonacci search, and golden search. As the golden search provides a similar performance to Fibonacci's, but is more straightforward to implement, that algorithm was chosen for the rest of this work. Similarly to the gradient, the method was directly implemented for the 7-dimensional problem, and reduced to two variables for the work of this section. Two main steps are followed by the method (note that the starting point, $\vec{x}_0$, and direction of the search, $\vec{s}$, are given as inputs to the method):

1. **Bracketing**: the search region is determined based on the starting point and the search direction, using an expansion factor $\gamma = 1.1$ and an initial increment $\Delta = 0.05\vec{x}_0$. Equation 4.4 is iterated upon with i until $f(x_i) > f(x_{i-1})$, defining the bounds of the golden search: $x_a = x_0$ and $x_b = x_i$ (selected x_i).

$$\vec{x}_i = \vec{x}_0 + \vec{s}\gamma^i\Delta \tag{4.4}$$

2. **Sectioning**: The sectioning is an iterative procedure which aims to reduce the interval $\vec{x}_a$ and $\vec{x}_b$ by computing $\vec{x}_c$ and $\vec{x}_d$, and redefining the bounds of the interval based on the objective value at points c and d. For $f(\vec{x}_c) < f(\vec{x}_d)$: $\vec{x}_b = \vec{x}_d$ and $\vec{x}_d = \vec{x}_c$, the interval is then reduced and point c is recomputed. Similarly, for $f(\vec{x}_c) > f(\vec{x}_d)$: $\vec{x}_a = \vec{x}_c$ and $\vec{x}_c = \vec{x}_d$, the interval is then reduced and point d is recomputed. This is iterated upon, until $\vec{h} < (\text{1E-7})\vec{x}_0$ (inequality in all components).

$$\vec{h} = \vec{x}_b - \vec{x}_a \tag{4.5}$$

$$\vec{x}_c = x_a + \frac{\vec{h}}{\Phi^2} \tag{4.6}$$

$$\vec{x}_d = x_a + \frac{\vec{h}}{\Phi} \tag{4.7}$$

No interpolation is performed as the magnitude of the residuals can be imposed to be arbitrarily small, rendering the interpolation unnecessary if the residuals are imposed to be lower than the model accuracy. The output value is taken as the average of the latest bounds of the search interval.

4.1.2.3 Classical Conjugate Gradient

With the gradient and line search methods, the Conjugate Gradient algorithm can be implemented. The first descent direction is taken opposite to the gradient (like in the steepest gradient algorithm), and the following ones are taken as,

$$x_{i+1} = \text{goldensearch}(x_i, d_i) \tag{4.8}$$

$$\vec{d}_{i+1} = -\vec{\nabla} f(x_{i+1}) + \left(\frac{||\vec{\nabla} f(x_{i+1})||}{||\vec{\nabla} f(x_i)||} \right)^2 \vec{d}_i \tag{4.9}$$

For a N dimensional problem, the descent direction is reset to $\vec{d} = -\vec{\nabla} f$ every N+1 steps, to improve convergence. The procedure is assumed to be converged if the vectorial residuals between two subsequent iterations is smaller than 1E-6 $\vec{x}_0$+1E-6 (the latter ensures that the program does not break if $\vec{x}_0$ has components being zero.

4.1.2.4 BFGS

Finally, the BFGS algorithm was also implemented because rank 2 quasi-Newton methods are known as the best general-purpose unconstrained optimization (hill climbing) methods. The BFGS method follows exactly the same structure as the Classical CG except that the search direction is updated using an inverse Hessian estimate, B, which is also updated at each iteration. The initial value of B is taken as the identity matrix. The following equations are iterated upon, until the same convergence criterion as mentioned for the Classical Conjugate Gradient method is reached.

$$\vec{d}_{i+1} = -B_i \vec{\nabla} f_i \tag{4.10}$$

$$\vec{x}_{i+1} = \text{goldensearch}(x_i, d_{i+1}) \tag{4.11}$$

$$s_i = \vec{x}_{i+1} - \vec{x}_i \tag{4.12}$$

$$y_i = \vec{\nabla} f_{i+1} - \vec{\nabla} f_i \tag{4.13}$$

$$B_{i+1} = B_i + \left(1 + \frac{y_i^T B_i y_i}{s_i^T y_i}\right)\left(\frac{s_i s_i^T}{s_i^T y_i}\right) - \frac{\left(s_i (y_i^T B_i) + (y_i^T B_i)^T s_i^T\right)}{s_i^T y_i} \tag{4.14}$$

4.1.2.5 Hessian Computation

Once the algorithm converges to a value, the Hessian of the function is computed using a Central Finite Difference scheme of the gradient in each of their components.

$$H_{ij} = \frac{\vec{\nabla} f(x_j + \delta)_i - \vec{\nabla} f(x_j - \delta)_i}{2\delta} \tag{4.15}$$

A (local) minimum has been found if the eigenvalues of the Hessian of the fitness function is positive-definite, which occurs if all its eigenvalues are positive.

4.1.3 Algorithm Performance Verification

The Himmelblau function was used to assess the performance of the implemented algorithms, as it is expected to be somewhat similar to the 7-dimensional space in terms of local minima distribution (a few, well spaced local optima). The BFGS and CG algorithms were both tested to ensure proper convergence to the closest local minimum of the function, with the results shown in Figure 4.1 which demonstrates that the algorithms indeed converge towards the points with zero gradient. While, saddle points are also found in some cases, an evaluation of the Hessian computation presented above directly reveals that the point found is a saddle point rather than a local optimum.

Additionally, it can be observed that the behaviour around saddle points can be different between the two algorithms, however. This can be a result of the size of the steps taken at each iteration.

4.2 L_1 - L_2 Optimisation

First, the reference design is optimised by only changing the lengths of the two poles. The results are shown in Figure 4.2a, showing how the constraints dictate the design space and the optimum for this simplified case. Note that the optimum was found using the BFGS described above, and not using the graph, which is only given for illustrative purposes (possible as only two variables are varied). Furthermore, note that the contours shown are the ones of the mass of the structure, rather than the fitness function described earlier. The optimised design can be found in Table 4.1, where the eigenvalues of the Hessian were found to be all positive.

Table 4.1: Optimised design for the length of both poles.

Variable	L_1 [m]	L_2 [m]	M [kg]
Value	8.6646	6.1883	409.2121

Table 4.2: Optimised design for the diameter of both poles.

Variable	D_1 [m]	D_2 [m]	M [kg]
Value	0.4691	0.1763	525.46

For this partially optimised design, constraints g_5 (diameter ratio, as the reference design already is on that constraint), g_{14} (first ray before the start of the road), and g_{15} (last ray after the end of the road) are active. This shows that the two lengths are mostly determined by the required illumination conditions, rather than the mechanical loading.

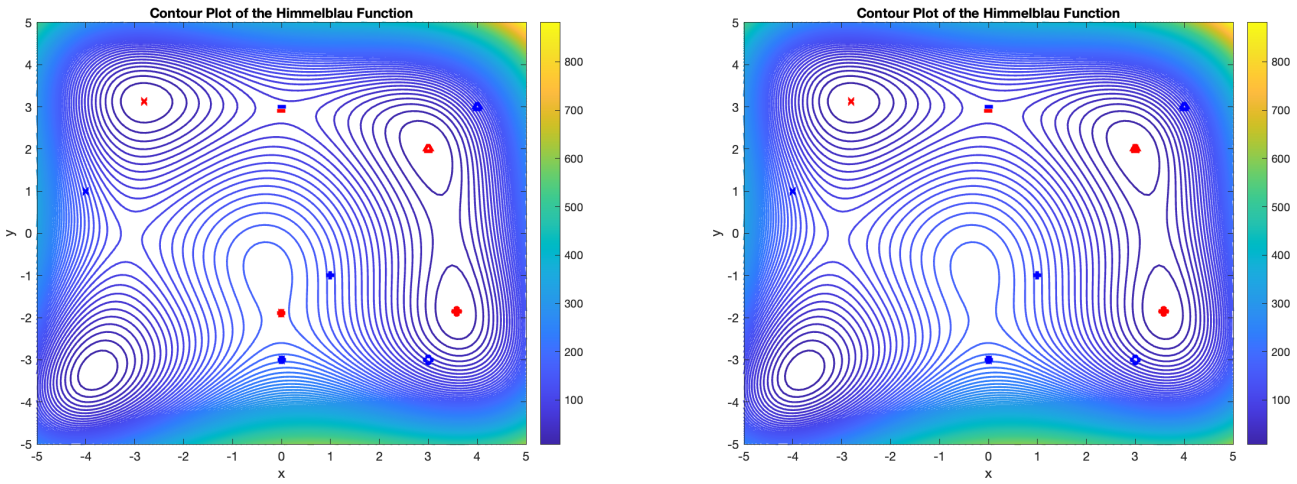

(a) BFGS. (b) Conjugate Gradient.

Figure 4.1: Performance of the BFGS and Conjugate Gradient methods implemented on the Himmelblau function. The red points are converged, the blue points are the starting values.

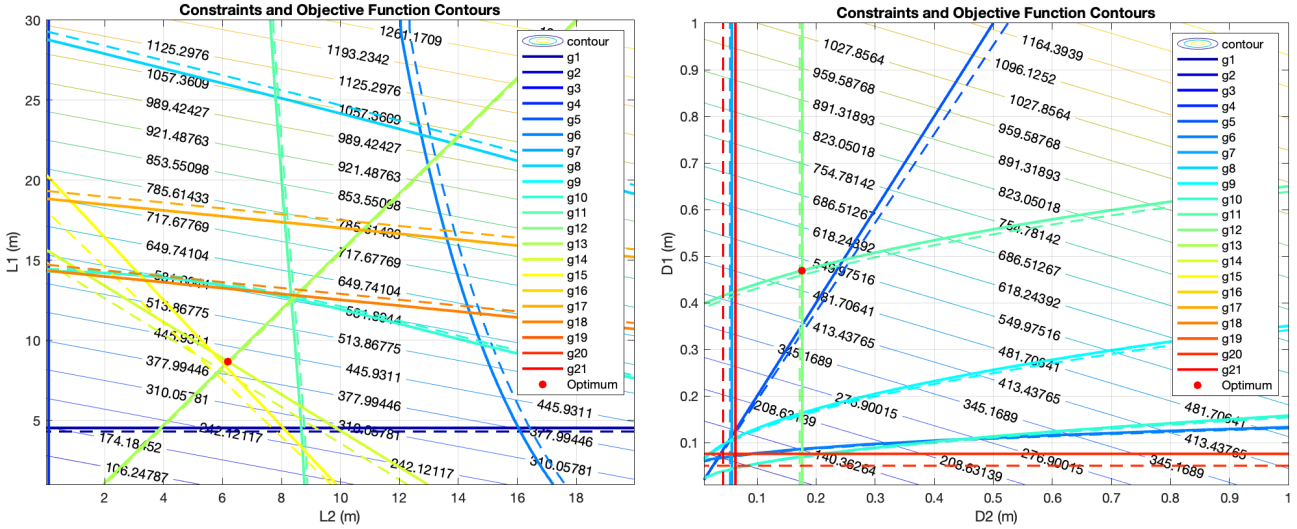

(a) L_1-L_2. (b) D_1-D_2.

Figure 4.2: Optimisation for the two pairs of variables, with the rest of the design variables fixed to the values given in Table 3.5.

4.3 D_1 - D_2 Optimisation

Following, the reference design is optimised by only changing the diameters of the two poles. The results are shown in Figure 4.2b, showing how the constraints dictate the design space and the optimum for this simplified case. Note that the optimum was found using the BFGS described above, and not using the graph, which is only given for illustrative purposes (possible as only two variables are varied). Furthermore, note that the contours shown are the ones of the mass of the structure, rather than the fitness function described earlier. The optimised design can be found in Table 4.1, where the eigenvalues of the Hessian were found to be all positive.

For this partially optimised design, constraints g_{11} and g_{12}, which relate to the planar deformation of the vertical and inclined poles respectively, are active. This shows that for a given thickness, the diameter is dictated by the deformations of the beams through the moment of inertia of the circular cross-sections.

4.4 Discussion of Results

It is clear that L_1 and L_2 have the largest influence on the mass of the system and dictate the majority of the shape of the structure. Only optimising for those two variables permitted to reduce the system's mass by $\approx$ 175kg, indicating that systems with much smaller masses could be reached through the interaction of the various design variables. This stems that (obviously), the current design is suboptimal. Furthermore, only two independent constraints (out of 21 used in the model definition) are active due to the small number of variables being optimised for. However, no other can be safely removed due to the effect of the five other

variables which were not varied in the present work. In general, two main conclusions can be drawn from this partial optimisation: the lengths of the poles are dictated by the illumination conditions, and their diameters are dictated by the allowed deformation under the wind loads. Additionally, it can be speculated that the thicknesses will be dictated by the stress conditions.
Following, the performance of the Classical CG, and BFGS methods were not formally compared to each other, because they converged both within a few iterations and the computational time was never considered as a constraint to obtain the requested results.

Global optimisation 5

During the choice of the algorithms for global optimisation, the choice for the algorithm depended on how well can an algorithm find the global optimums. It was expected that with seven different design variables, multiple local minima may be present. Therefore, to find global optima with higher probability - priority was given to the biologically inspired algorithms, due to their randomness involved in those algorithms. More specifically particle swarm and genetic algorithm (GA) were used. To further certify the results, for each algorithm run, local optimisers were used on the converged value (BFGS and Sequential Quadratic Programming (SQL)).

5.1 Himmelblau Test

As a first step, the algorithms were tested on the Himmelblau function. This was done to understand how all of the algorithms work and whether they can be used to find optimal values, on a simpler objective function which only involves two variables. All of the algorithms were able to find one of the local optima.
However, it was interesting to point out that by changing the number of particles or by changing the type of crossover function (in case of GA), the found optima point could differ as seen in the Figure 5.1. Furthermore, as expected the accuracy of results has been increased whenever the population or number of generations was increased, at the cost of the computational time, however. On the other hand, the computational time could be reduced by the introduction of local optimisation such as the in-built Matlab function 'fmincon' which performs the SQL, to determine the optimum based on a pre-converged population.

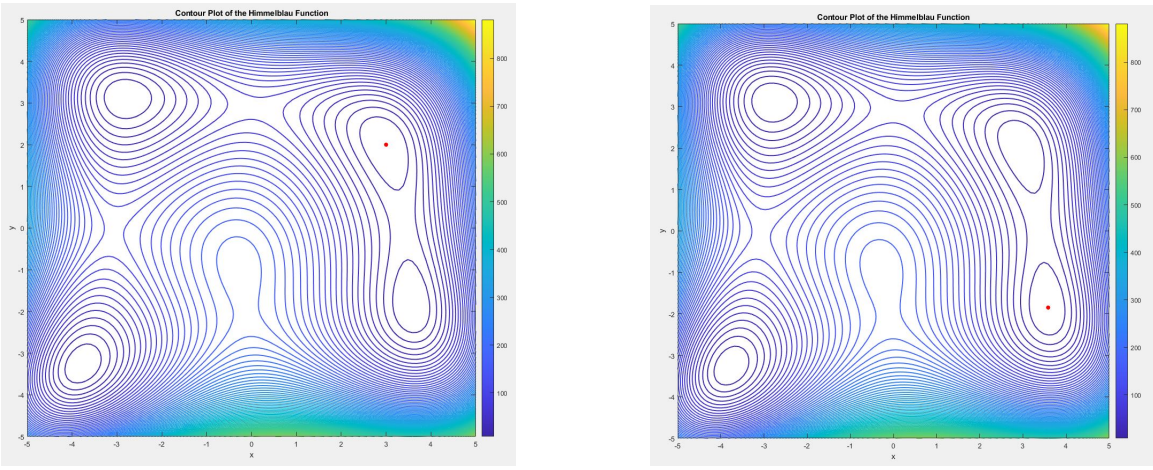

(a) Particle Swarm with particle population of 100 (b) Genetic algorithm with heuristic crossover

Figure 5.1: Himmelblau optimisations, with red being the local optima found.

5.2 Algorithms Setup

To implement either of the algorithms, as a first step the upper and lower bounds were set. This was done to specify the search range for the algorithms, otherwise, the computational time was too long and there was a chance that the results found are in the infeasible domain. In order to make sure that the program does not crash due to division by zero, all of the values in the lower bound are above zero. All of the bounds can be seen in the Table 5.1.

Table 5.1: Lower and Upper Bounds for the algorithms

Variable	D_1	L_1	t_1	D_2	L_2	t_2	α (rad)
Lower Bound	0.01	4	0.0005	0.01	0.1	0.0005	$\frac{1}{180}\pi$
Upper Bound	0.5	25	0.1	0.5	10	0.1	$\frac{50}{180}\pi$

To implement a particle swarm, the fitness function needed to be used since the function of implementing the non-linear constraints is absent in the optimisation toolbox for this algorithm. Therefore, a high penalty of $E10$ has been selected for the fitness function to find realistic bounds imposed by the constraints. Furthermore, the initial runs were taking significant computational time, therefore the swarm size has been restricted to 100 particles for all of the future runs. Interestingly, the implementation of Sequential Quadratic Programing (SQL) as a local optimiser did not influence the computational time and the number of iterations stayed similar.

For the genetic algorithm, the nonlinear constraints were implemented by implementing a function $nonlcon$ which contained all of the inequality constraints g and equality constraints h, the latter being an empty matrix for this problem. Considering that the $nonlcon$ function was used, the regular objective function has been used instead of the To use the full advantage of such an algorithm, the mutation and the crossover functions were turned on, to include randomness in the search.

To find global optima, other direct search algorithms such as the Nelder-Mead simplex method were considered for this optimisation problem. However, such a method was producing results with highly negative diameters and masses, subsequently violating the constraints imposed. Therefore, this method was not investigated in further results.

5.2.1 Algorithms Comparison

For testing purposes, some of the runs were made without the use of SQL. What was often happening is that the genetic algorithm was unable to find the local optima with the same number of particles as the particle swarm, and the same starting search point. Instead, the genetic algorithm was finding a value in the region of the local optima. The computational time for the particle swarm, however, was longer than for the genetic algorithm even though the average change tolerance value specified was the same for both algorithms (being $1e-6$).

However, with the use of SQL both of the genetically inspired algorithms were producing the same results. However, this time genetic algorithm had four times shorter computational time compared to the particle swarm. Computational time was found by introducing the variable $tEnd$ in the code. This suggests that the genetic algorithm is more suitable for identifying the region of the local optima rather than the particle swarm. However, later a local optimiser is needed to use the reduction in computational time to the user's advantage.

From these findings, the sensitivity analysis of constant variables (Section 5.5) was performed using a hybrid genetic algorithm and SQL as a local optimiser. However, there were instances when either of the two algorithms was not finding the optima and the other one did. In those cases, a different randomiser has been implemented, by using a different setup in Matlab's $'rng'$ function or by using a different population/type of crossover (in the case of GA), and the optimal result was obtained.

5.3 Initial Results

In the first runs, with either particle swarm or the genetic algorithm, the results produced did not look realistic. The algorithms were able to find local optima which resulted in the final mass of 0.5 kg. This acted as an indication that some of the constraints were neglected since the diameters of the vertical and inclined poles were about 1 cm each. As a possibility, it was figured that the streetlight is free to deflect how much it wants preventing it from failing. Therefore, the deflection constraints have been added, seen in Subsection 2.5.2, and all of the optimisations have been repeated. Results in Chapter 4, include these constraints too.

Further optimisation tries were implemented and at certain field-of-view angles, reasonable results for the final mass were found. For instance for values of FoV at 50 degrees as seen in Table 5.2. However, at the higher FoV angles the algorithm found a loophole in the model, and gave solutions with the minimal length of the inclined pole at a high angle. Furthermore, the vertical length was constrained only by the L_{truck}. Such results produced a streetlight's mass of only 3 kg and were considered unrealistic. Not only the mass is too low, but also if the truck passes by the shadow will cover the entire road which is undesired therefore another new constraint has been introduced.

Finally, it was unreasonable that the diameter of the inclined pole was in some simulations larger than the main vertical pole. Therefore, a new constraint g_{16}, Equation 2.38, was implemented to prevent such a result from happening. All of these changes were applied and implemented for both simplified and global optimisations.

Table 5.2: Old results for FOV 50 and FOV 60, before the shadow constraint implementation.

FoV (deg)	$D1$ (m)	$L1$ (m)	$t1$ (m)	$D2$ (m)	$L2$ (m)	$t2$ (m)	α (rad)	Mass (kg)
50	0.7000	11.4140	0.0013	0.0101	0.1382	0.0008	0.5396	104.8046
60	0.1203	4.5263	0.0005	0.0100	0.1000	0.0005	0.7847	2.7643

5.4 Investigation of Obtained Optimum

After making sure the algorithms are working correctly and implementing previously neglected constraints, the global optimisation finally started producing reliable results. The results are sensitive to the changes in constraints or the constants, the main ones being specified in Table 5.3. To understand whether the results by the algorithm make sense, a Table 5.4 of reference values has been created for comparison.

The results obtained for the global optimisation can be seen in Table 5.5. Throughout, the testing of the global optimisation, the algorithm always picked the maximum allowed diameters. This makes sense since a higher diameter allows for a higher moment of inertia while not increasing the thickness of the structure, which adds mass. The final mass value makes sense by comparing it with the reference values presented in Table 5.4.

Table 5.3: Constant values for the global optimisation

Category	Value
Mechanical Modelling	
FOV_light	75 [deg]
w_lane	5 [m]
w_road	$w\_lane \times 3$ [m]
B_req	5.86×10^{-3} [W/m^2]
P_light	30 [W]
Wind Modelling	
v_max	32.6 [m/s]
z_r	30 [m]

Table 5.4: Reference Design Values [11]

Parameter	Value	Unit
$L1_{\text{ref}}$	12	m
$D1_{\text{ref}}$	0.3	m
$t1_{\text{ref}}$	0.0063	m
$L2_{\text{ref}}$	1.2	m
$D2_{\text{ref}}$	0.3	m
$t2_{\text{ref}}$	0.0063	m
α_{ref}	10	rad
$L_{\text{mount\_to\_L1\_ratio}}$	0.95	-
m_{ref}	300	kg

Table 5.5: Final optimization results

Parameter	$D1$ (m)	$L1$ (m)	$t1$ (m)	$D2$ (m)	$L2$ (m)	$t2$ (m)	α (rad)	Mass (kg)
Value	0.5000	8.5278	0.0007	0.2500	5.9923	0.0008	0.1889	**40.5979**

By looking at the constraints stated in Table 5.6, since all of the values are negative, none of the constraints are violated by the algorithm. Suggesting that a feasible design space was still left available, despite an introduction of 22 different constraints. However, after iterations in the global optimisation, some of the constraints became redundant, which can be improved in the future works of the code. For instance, the large value for g_4 shows redundancy, g_4 was constraining in previous runs to make sure that there is enough space to place a lamp on the inclined pole. However, with the introduction of shadow constraint (g_{15}), that parameter became more limiting.

Table 5.6: Constraints for the final optimization

g_1	g_2	g_3	g_4	g_5	g_6	g_7	g_8	g_9	g_{10}	g_{11}
-0.884	-0.400	-0.600	-58.9	0	-0.994	-0.472	-0.964	-0.307	-0.823	0.032

g_{12}	g_{13}	g_{14}	g_{15}	g_{16}	g_{17}	g_{18}	g_{19}	g_{20}	g_{21}	g_{22}
-0.057	-1.316	-1E-4	0.000	0.000	-1.303	-2.821	-1.116	-0.099	-0.097	-0.000

For this final optimisation run, the most limiting constraints are the light illuminating the start of the road (g_{13}), pole deflections (g_{10} and g_{11}), the shadow angle created by a passing truck's shadow (g_{15}), and the diameter ratio (g_{21}). The inclined pole's length ($L2$) is now rather long, especially if compared to reference values in

Table 5.4. The potential reason for that is the shadow constraint which forces the light source to be above the road, and then g_{13} stops the length from growing so that rays still hit the beginning of the road.

The final mass of 40.6 kg is considered a realistic result since some reference mass values were found within that range. Furthermore, most streetlight poles do not have such a large diameter as stated in this problem. This is due to the fact that half a meter diameter may be difficult to attach to the ground, therefore in reality slimmer and thicker designs may be preferred. For instance, if the upper bound is set to $0.3m$ for D_1, the final mass found is $87.8kg$ which is closer to the reference values of a streetlight.

Another reason for a rather light design is potentially a low safety factor taken, and the use of the assumption that wind force at the ground is zero. To test these factors and how they influence the design, a sensitivity analysis has been performed on those and other variables.

5.5 Sensitivity Analysis

For the sensitivity analysis, the main parameters from the constants that may influence the results are the lamp's field of view (FoV), the road's width and the reference height (z_r) for the wind profile. This section will analyse how much a change of a constant by 10% would change the final mass result.

However, firstly, the change of FoV over a large range of values is performed as seen in Table 5.7. The results are for a two-lane road and were used to check if the shadow constraint (g_{15}) fails for shorter road width. However, it gives a good insight into the fact that the algorithm always tries to take the maximum width, and only then thickness is increased if needed. For low FoV, to reduce the loads the algorithm tries to shorten the inclined pole and increase the angle. At higher FoV the parameter becomes less sensitive, but at FoV 90 degrees algorithm produces an anomaly, due to constraint g_{15} being incompatible with the 2-lane road.

Table 5.7: Results for Testing Different FoV (in degrees) for a 2 lane road

FoV (deg)	$D1$ (m)	$L1$ (m)	$t1$ (m)	$D2$ (m)	$L2$ (m)	$t2$ (m)	α (rad)	Mass (kg)
30	0.5000	17.8582	0.0221	0.0171	1.2409	0.0005	0.2648	**1920.3**
50	0.5000	10.6912	0.0019	0.2350	5.0984	0.0005	0.0903	**108.8746**
75	0.5000	8.2714	0.0006	0.2500	6.2322	0.0009	0.1417	**38.4372**
90	0.4999	7.8279	0.0005	0.2499	6.1353	0.0008	0.3070	**30.6614**
120	0.5000	7.6477	0.0005	0.2500	6.6284	0.0010	0.1147	**34.0280**

Moving on to the sensitivity analysis, the FoV parameter still remains a highly sensitive variable, as seen in Table 5.8. A change of FoV by 10% creates a change of 62% for the final value. The reason for that is that at lower FoV the algorithm makes the vertical pole taller to cover the road, but due to higher loads above, the structure becomes thicker to sustain higher loads. Meaning that the choice of new light sources with high FoV would significantly reduce the material used for streetlight manufacturing.

Table 5.8: Sensitivity analysis on the FoV influence

FoV (deg)	$D1$ (m)	$L1$ (m)	$t1$ (m)	$D2$ (m)	$L2$ (m)	$t2$ (m)	α (rad)	Mass (kg)
67.5	0.500	9.694	0.0012	0.250	5.335	0.0005	0.226	**65.771**
75	0.5000	8.5278	0.0007	0.2500	5.9923	0.0008	0.1889	**40.598**
82.5	0.500	7.894	0.0005	0.250	6.249	0.0009	0.219	**32.752**

Wind's reference height (z_r) is also a sensitive variable producing almost a 10% difference to the final mass value, as seen in Table 5.9. The reason for this change is rather obvious, the lower the reference height for the maximum velocity, the denser the wind force profile and the more force is exerted on the pole. The sensitivity analysis of this parameter signifies the importance of initial wind modelling, as any mistake in that step would lead to significant design changes for the streetlight or other structures experiencing wind. Too low of a reference height, can also lead to an infeasible design as seen in Table A.1 at $5m$.

The road width is a sensitive parameter causing a 12% increase in the final mass value if the width is increased by 10%, as seen in Table 5.10. Unlike with reference height sensitivity analysis, the results change significantly with the lengths of the poles for the length of the road. This is due to the illumination constraints playing a role since the inclined pole needs to be longer to illuminate a wider road, hence there is an increase in the final mass.

Table 5.9: Results for Testing Different Reference Heights (in meters)

z_r (m)	$D1$ (m)	$L1$ (m)	$t1$ (m)	$D2$ (m)	$L2$ (m)	$t2$ (m)	α (rad)	**Mass**
27	0.500	8.5277	0.0008	0.250	5.9923	0.0008	0.189	**44.4012**
30	0.5000	8.5278	0.0007	0.250	5.9923	0.0008	0.1889	**40.598**
33	0.500	8.5277	0.0007	0.250	5.9923	0.0007	0.189	**37.4720**

Table 5.10: Results for Testing Different Road Widths (in meters)

Road Length (m)	$D1$ (m)	$L1$ (m)	$t1$ (m)	$D2$ (m)	$L2$ (m)	$t2$ (m)	α (rad)	**Mass**
13.5	0.500	8.27	0.0006	0.250	6.23	0.0009	0.142	**38.436**
15.0	0.5000	8.5278	0.0007	0.250	5.9923	0.0008	0.1889	**40.598**
16.5	0.500	8.87	0.0008	0.250	5.72	0.0007	0.240	**45.357**

Regarding the required brightness (B_{req}) and the safety factor (SF), these constants do not change the final mass, as seen in Table A.3 and Table A.2. In the case of SF the final mass has not been changed since the restraining constraints were not related to the structural stress. And in the case with B_{req}, the power of the light source is sufficient enough for the minimum illumination required.

5.6 Conclusion and Recommendations

From the final results, it can be seen that both of the biologically inspired search algorithms can find the global optimum solutions. If the user wishes to use an algorithm without a local optimiser, then the particle swarm produces results closer to the global optimum than the genetic algorithm. However, if a hybrid of a local optimiser (SQL or BFGS) and a search algorithm is used, then the results obtained are the same for both algorithms compared. The hybrid of SQL and the genetic algorithm was found to be the most optimum way of searching for the global optimum due to the shorter computational time. Other direct search methods like Nedler-Mead Simplex did not produce realistic results.

The implementation of complete optimisation worked well for spotting flaws in the model. The production of unrealistic results discussed in Section 5.3 resulted in the inclusion of new constraints which were overlooked in the initial model. To spot these flaws it was helpful to have reference design values of other streetlights.

The final result of 40.6 kg for the streetlight made sense, and all of the constraints were satisfied leading to a positive result in this optimisation problem. While the inclined pole length is on the high side, the other design variables found are in the expected range, showing that a sensible set of constraints and a successful optimisation algorithm was selected. From performing the sensitivity analysis, it was noted that the program is highly sensitive to the initial model parameters set, which need to be carefully selected by the user for optimal results. Especially picking a light source with high FoV would result in a significant mass reduction for the streetlight.

For recommendations, the algorithm almost always picked pole diameters $D1$ and $D2$ at the upper bound to minimise the mass. Potentially to simplify the objective function for future runs, it can be a good idea to keep those values constants. This would reduce the work to check for monotonicity and the algorithm may need to do fewer calculations. Hence improving computational time.

References

[1] Jividen Law Offices. “Street lighting and car accidents.” (2023), [Online]. Available: https://www.jividenlaw.com/blog/street-lighting-car-accidents/ (visited on 06/03/2023).

[2] AZO Material. “Aluminum - advantages and properties of aluminum.” (2023), [Online]. Available: https://www.azom.com/properties.aspx?ArticleID=1446 (visited on 06/30/2023).

[3] Koninklijk Nederlands Meteorologisch Instituut (KNMI), *Windschaal van beaufort*, https://www.knmi.nl/kennis-en-datacentrum/uitleg/windschaal-van-beaufort, Accessed 2023, May 16.

[4] E. Abayomi, “1.11 - hiv/aids disease burden complex in south africa: Impact on health and environmental resources, and vulnerability to climate,” in *Climate Vulnerability*, R. A. Pielke, Ed., Oxford: Academic Press, 2013, pp. 125–143, ISBN: 978-0-12-384704-1. DOI: https://doi.org/10.1016/B978-0-12-384703-4.00125-8. [Online]. Available: https://www.sciencedirect.com/science/article/pii/B9780123847034001258.

[5] J. Touma, “Dependence of the wind profile power law on stability for various locations,” *Journal of the Air Pollution Control Association*, vol. 27, pp. 863–866, 1977.

[6] S. F. Hoerner, *Fluid-Dynamic Drag*. Bricktown, New Jersey: Hoerner Fluid Dynamics, 1965.

[7] R. Hibbeler, *Mechanics of Materials, SI Edition*, 10th. Pearson, 2018, ISBN: 9781292178202.

[8] JPE Innovations. “Beam theory - bending.” (Year the website was last accessed), [Online]. Available: https://www.jpe-innovations.com/precision-point/beam-theory-bending/.

[9] F. P. LED. “Watts, lumen, electricity cost, and street light.” (Year the website was last accessed), [Online]. Available: https://www.finepixeled.com/watts-lumen-electricity-cost-street-light/.

[10] MK Lights. “Standard for lighting design of urban road.” (Year the website was last accessed), [Online]. Available: https://www.mklights.com/BLOGS/standard-for-lighting-design-of-urban-road.html.

[11] LightMart. “40 foot aluminum street light pole with 4 foot mast arms, 8 inch diameter, 0.250 inch wall thickness.” (2023), [Online]. Available: https://www.lightmart.com/40-foot-aluminum-street-light-pole-with-4-foot-mast-arms-8-inch-diameter-0-250-inch-wall-thickness/ (visited on 06/23/2023).

Additional Information A

This appendix provides additional information to support the understanding of the reader on specific parts of the report.

A.1 Objective Function Derivatives

$$\frac{df}{dL_1} = 1.2\left(\left(\frac{D_1}{2}\right)^2 - \left(\frac{D_1}{2} - t_1\right)^2\right)\pi\rho \quad \text{(A.1a)} \qquad \frac{df}{dD_1} = 1.2\left(\frac{D_1}{2} - \left(\frac{D_1}{2} - t_1\right)\right)\pi L_1\rho \quad \text{(A.1b)}$$

$$\frac{df}{dt_1} = 2.4\left(\frac{D_1}{2} - t_1\right)\pi L_1\rho \quad \text{(A.1c)} \qquad \frac{df}{dL_2} = \left(\left(\frac{D_2}{2}\right)^2 - \left(\frac{D_2}{2} - t_2\right)^2\right)\pi\rho \quad \text{(A.1d)}$$

$$\frac{df}{dD_2} = \pi\rho\left(\frac{D_2}{2} - \left(\frac{D_2}{2} - t_2\right)\right)\left(L_2 + \left(\frac{D_2}{2}\right)\tan(\alpha)\right) + \left(\left(\frac{D_2}{2}\right)^2 - \left(\frac{D_2}{2} - t_2\right)^2\right)\frac{\pi\tan(\alpha)\rho}{2} \quad \text{(A.1e)}$$

$$\frac{df}{dt_2} = \left(\frac{D_2}{2} - t_2\right)\pi L_2\rho + \left(\frac{D_2}{2} - t_2\right)\pi\left(\frac{D_2}{2}\right)\tan(\alpha)\rho \quad \text{(A.1f)}$$

$$\frac{df}{d\alpha} = \left(\left(\frac{D_2}{2}\right)^2 - \left(\frac{D_2}{2} - t_2\right)^2\right)\frac{\pi\rho D_2}{2\cos(\alpha)^2} \quad \text{(A.1g)}$$

A.2 Sensitivity Tables

Table A.1: Results for Testing Different Reference Heights (in meters) for a 2 lane road

zr (m)	$D1$ (m)	$L1$ (m)	$t1$ (m)	$D2$ (m)	$L2$ (m)	$t2$ (m)	α	Mass (kg)
5	—	—	—	—	—	—	—	—
10	0.500	8.267	0.002	0.250	6.237	0.002	0.141	**97.014**
20	0.500	8.269	0.001	0.250	6.234	0.001	0.141	**54.174**
30	0.500	8.271	0.001	0.250	6.232	0.001	0.142	**38.437**
50	0.489	8.582	0.001	0.244	5.947	0.001	0.197	**27.508**

Table A.2: Results for Testing Different Brightness Requirements (in W/m^2)

Brightness (W/m^2)	$D1$ (m)	$L1$ (m)	$t1$ (m)	$D2$ (m)	$L2$ (m)	$t2$ (m)	α	**Mass**
5.27 E-3	0.500	8.53	0.0007	0.250	5.99	0.0008	0.189	**40.5963**
5.86 E-3	0.5000	8.5278	0.0007	0.250	5.9923	0.0008	0.1889	**40.598**
6.45 E-3	0.500	8.53	0.0007	0.250	5.99	0.0008	0.189	**40.5979**

Table A.3: Results for Testing Different Safety Factors for 2 lanes

SF	$D1$ (m)	$L1$ (m)	$t1$ (m)	$D2$ (m)	$L2$ (m)	$t2$ (m)	α	**Mass**
1.35	0.500	8.2714	0.0006	0.250	6.2323	0.0009	0.142	**38.4360**
1.5	0.500	8.2714	0.0006	0.250	6.2322	0.0009	0.142	**38.4372**
1.65	0.500	8.2714	0.0006	0.250	6.2323	0.0009	0.142	**38.4360**
2	0.500	8.2714	0.0006	0.250	6.2323	0.0009	0.142	**38.4360**

A.3 Matlab Code

The Matlab code developed in throughout this project was added as a zip file to the Brightspace submission.